Dual-Pace Transient Heat Conduction in Vertically Aligned Carbon Nanotube Arrays Induced by Structure Separation

Yangsu Xie[a], Hamidreza Zobeiri[b], Liping Xiang[a], Gyula Eres[c,*], Jianmei Wang[d,*], Xinwei Wang[b,*]

[a] College of Chemistry and Environmental Engineering, Shenzhen University, Shenzhen 518055, Guangdong, P. R. China

[b] Department of Mechanical Engineering, 271 Applied Science Complex II, Iowa State University, Ames, IA 50011

[c] Oak Ridge National Laboratory, Materials Science and Technology Division, Bldg 4100, MS 6118, Oak Ridge, TN, 37831, USA

[d] School of Power and Mechanical Engineering, Wuhan University, Wuhan, 430072, China

Abstract: Vertically aligned arrays of carbon nanotubes (CNTs) are attractive for a wide range of macroscopic applications which can exploit the remarkable properties of individual nanotubes. In this work, an abnormal behavior of CNT bundles in heat conduction is discovered under the transient electro-thermal characterization. The measured voltage change over the sample shows a dual-pace thermal response (DTR), which could not be fitted using a single thermal diffusivity. Instead, two thermal diffusivities are determined from the DTR phenomenon. Three rounds of cryogenic experiments are conducted to investigate the physics behind DTR phenomenon. It starts to emerge when the temperature is reduced to a certain level. After two rounds of cryogenic experiments, the DTR phenomenon becomes permanent over 295 K to 10 K. The nano-scale

* Corresponding authors. G.E.: Tel: 001-865-574-5494, E-mail: eresg@ornl.gov; J.W.: Tel: 13317101217, E-mail: jmwang@whu.edu.cn; X.W.: Tel: 001-515-294-8023, Email: xwang3@iastate.edu

structure separation induced by the increased thermal strain leads to structure separation, which results in two parallel heat conduction paths responsible for the DTR phenomenon. By building a new parallel heat transfer model taking both the transient and steady-state electrical and thermal response into consideration, the area ratio of separated CNTs is determined. This result uncovers the existence of coiled morphology and nano-structure evolution of CNTs under low temperatures and its effect on thermal and electrical transport, especially on their transient behaviors. Knowledge of the thermal transport in these CNTs arrays is important considering the temperature and transient thermal response strongly affect their mechanical, optical, and electrical behaviors.

1. Introduction

Vertically aligned arrays of carbon nanotubes (VACNTs) are attractive for a wide range of macroscopic applications which can exploit the remarkable properties of individual CNTs.[1] Application of VACNTs in thermal interface management,[2-4] thermionic and field-emission electron sources,[5] strain and temperature sensors,[6] loudspeakers,[7, 8] incandescent displays,[9] energy conversion[10] and storage[11], etc. have been widely reported. Thermal chemical vapor deposition (CVD) is a technique capable of directly producing vertically aligned arrays of CNTs on various substrates,[12-14] which uses thermal energy to promote the reaction between the carbon source and the catalyst at high temperature by thermal decomposition. In terms of the theoretical limits of electrical and thermal conductivities for individual CNTs, alignment of CNTs is an important factor. However, in most cases, CNTs are not perfectly aligned in VACNTs,[15] where helical and zigzag morphology are usually observed. Wang *et al*. investigated the evolution of straight tubes and coiled tubes during CVD process and found that the coiled morphologies were driven by the competing factors of collective growth and spatial constraints.[16] Due to their helical morphology, helical CNT bundles exhibit different physical properties, such as superelasticity, high specific strength, chirality, and electromagnetic cross-polarization characteristics,[17] which bring them advantages in applications such as field emission,[18] microwave absorbing,[19] and strain sensor[20]. Knowledge of thermal transport in these micro/nanoscale structures has become indispensable considering the temperature and thermal response of materials strongly affect their mechanical, optical, and electrical properties.

The random alignment and curvatures of CNTs provide significant phonon and electron scattering sites. Furthermore, the effect of thermal contact resistance is also significant in CNTs network.[21-

24] As a result, the thermal conductivity (k) of VACNTs arrays is much lower than the intrinsic k of CNTs. The transient electro-thermal (TET) technique,[25, 26] thermal bridge,[27] 3ω method,[28] laser-flash,[29] and Raman method etc.[30-33] have been used for thermal characterization of CNTs materials. Bauer *et al*. measured k of vertically aligned CNT arrays to be only 49- 79 W/m·K.[34] Other works reported even lower values (<25 W/m·K).[35, 36] k of MWCNT films were reported to be about 15 W/m·K by using the photothermal reflectance technique.[37] For SWCNTs mats, k was measured to be about 35 W/m·K according to Hone *et al.*[38] To study the effect of thermal contact resistance, T-type method,[39] micro-heater/sensor method,[40] as well as laser-flash Raman mapping method [41] have been used for characterizing the thermal contact resistance between individual carbon tubes. In addition, it should be noted that the porosity level and density of CNT samples also cause differences in k. The density of a disk-shape MWCNT fabricated by spark plasma sintering (SPS) from 800 to 2000 ^{o} C were from 350 to 1450 kg/m^3.[42] The apparent densities of randomly aligned multi-walled CNTs buck papers were calculated at 459 and 543 kg/m^3[30]; while for MWCNTs bundles, it was reported to be 116-234 kg/m^3.[35] By taking the porosity effect into consideration, Xie *et al*. reported the intrinsic k of CNT walls in CNTs bundles to be as high as 754 W/m·K after the thermal annealing treatment.[26]

Compared with thermal conductivity, thermal diffusivity tells more about the CNT-CNT contact effect and curvature effect since it is less affected by the porosity level. Guo *et al*. found that the curvature morphology reduced the thermal diffusivity (α) of multiwalled CNT bundles by 10 folds by elongating the heat propagation route from first order estimation based on the alignment.[43] Xie *et al*. calculated the intrinsic k of CNT walls from the heat transfer path aspect, where the 3D

ratio of the curvature length of CNTs over the straight-line length was estimated.[26] Deng *et al.* studied the thermal diffusivity and conductivity of carbon nanocoils from 290 to 10 K and uncovered a correlation between α and the line diameter.[44] To have a better understanding of phonon scattering mechanisms, the temperature-dependent thermal reffusivity (the reciprocal of thermal diffusivity) has been proposed and studied.[45] It is an intrinsic property of materials which can be used to directly characterize the phonon transfer resistivity. It was found that as temperature goes down, the thermal reffusivity of normal carbon materials including graphite, graphene foam, and carbon nanocoils decreased and finally reached a residual value at the 0 K limit, whose value was dependent on the structural domain size of materials.[45-48] However, for composite materials such as the VACNTs arrays, where large amount of inter-tube contacts exist, the behavior of the phonon scattering can be more complex. In addition, due to the existence of both straight and coiled morphologies of CNTs, the interplay of the two morphologies is expected to be responsible for macroscopic thermal and electrical behaviors.[49, 50]

In this work, an abnormal thermal behavior of CNT bundles in heat conduction is discovered by using the TET technique. Upon step DC current heating, the sample experiences a first fast resistance decay and then a slow one, meaning dual-pace thermal response (DTR). Contrast to normal sample's exponential variation with a single time constant, DTR cannot be simply interpreted by normal transient heat conduction. This phenomenon is impossible to observe in other heat conduction studies, especially studies using the steady state method. To uncover the physics of DTR, three rounds of cryogenic experiments are conducted to investigate the thermal diffusivity, thermal conductivity, and specific heat from 295 K to 10 K. The unique structure of the CNT bundles constitutes parallel distinct thermal transport paths which result in DTR. A new

parallel heat transfer model is developed to interpret the observed DTR phenomenon by taking both the transient and steady state electrical and thermal response into consideration based on the micro-structure evolution of VACNT arrays.

2. Material Synthesis and Structure Characterization

The VACNTs is grown by chemical vapor deposition (CVD) on a Si 100 wafer using a two-layer metal catalyst film consisting of 10 nm of Al and 1 nm of Fe. The experimental details can be found in the literature.[51] Briefly, the catalyst film is deposited on a Si wafer using electron beam evaporation through a shadow mask with periodic holes of 200 μm diameter. Acetylene is used as the carbon source gas, which is flowed concurrently with ferrocene sublimated from a thermal source in the CVD process. After that, a vertically aligned array sample of 4.5 mm thickness is obtained. The resulting CNTs are aligned vertically and formed into bundles by Van der Waals forces, where continuous CNT bundles can be easily drawn from the VACNTs. MWCNT bundles with a diameter of about 200 μm are then harvested from the array for the subsequent thermal transport study. The micro-structure of the as-prepared CNT bundles is observed under scanning electron microscope (SEM). As shown in Fig. 1(a), a good alignment along the axial direction under low magnification can be observed. However, the coexistence of two morphologies of CNTs, one being relatively straight whereas the other taking regularly coiled morphology, is also evident under higher magnifications [Fig. 1(b)]. These morphologies are resulted from the competing effects of collective growth and spatial constraints during the CVD process.[16]

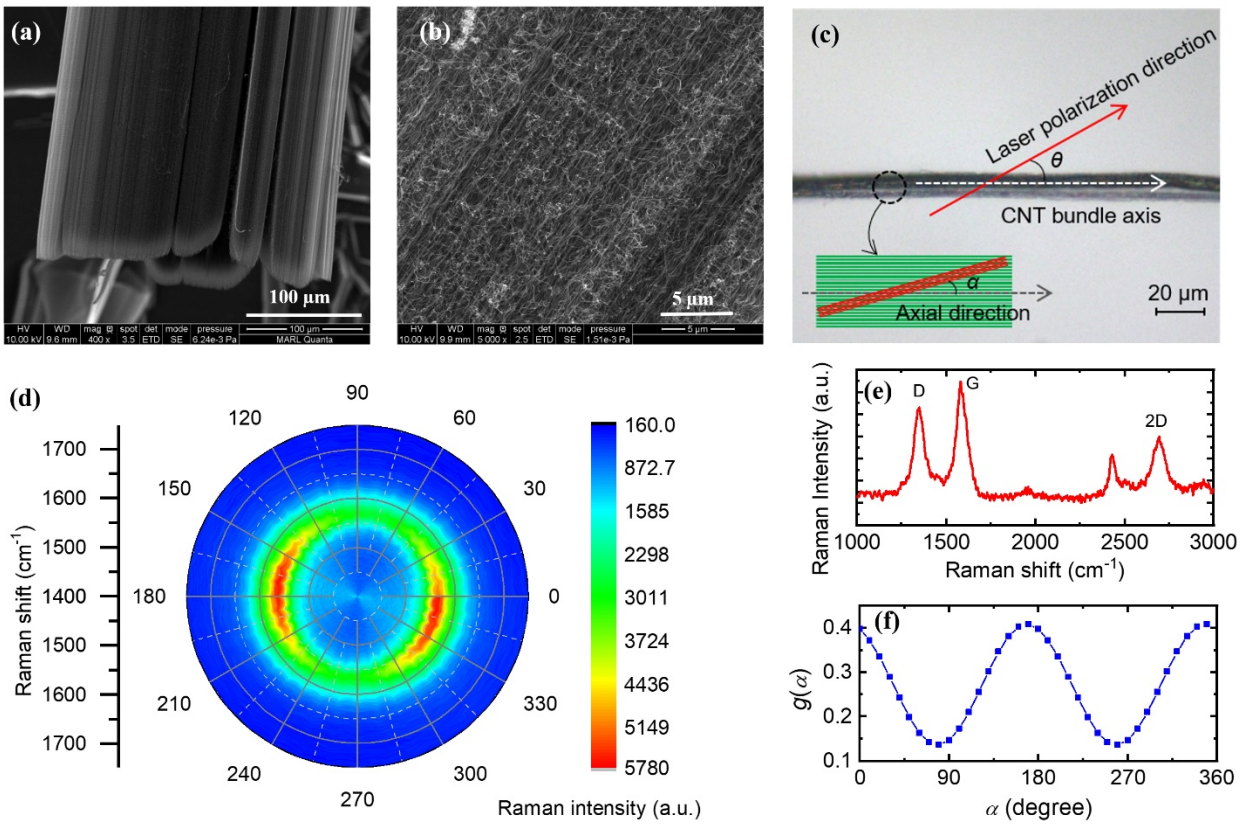

Figure 1. (a)-(b) SEM images of the CNT bundles under different magnifications. (c) The schematic of the polarized Raman experiment. (d) The polar contour of Raman signals against θ in the range of 1400 to 1750 cm^{-1} under 532 nm CW laser irradiation. (e) One of the Raman spectrum of CNT bundles. (f) The normalized function g(α) against the polar angle.

In order to investigate the orientation distribution of CNTs inside the bundle, a polarized Raman experiment is performed. Figure 1(c) shows the CNT bundle and polarization direction of the continuous wave (CW) laser. Here, θ is the polarization angle, and α represents the orientation of each nanotube inside the bundle [inset of Fig. 1(c)]. It has been proved that the light polarization-dependent absorption of CNT is proportional to $\cos^2(\theta-\alpha)$ [52], which shows that the light absorption by a nanotube reaches maximum when it is parallel to the light polarization direction. Knowing that Raman intensity is higher when the light absorption is higher, using the light

absorption relationship with polarization and individual nanotube's orientation, the orientation distribution function $g(\alpha)$ of CNTs inside the bundle affects the polarized Raman intensity as

$$f(\theta) = \int_{0^\circ}^{360^\circ} g(\alpha)\cos^2(\theta-\alpha)d\alpha, \quad (1)$$

where $f(\theta)$ is directly proportional to the Raman intensity at angle θ. Function $g(\alpha)$ represents the probability of finding nanotubes at different direction α with respect to the bundle's axial direction. Here, using the polarized Raman experiment, we can find the polarized Raman intensity of *G* peak of CNT bundle against θ. Figure 1(d) shows the polar contour of Raman spectra of CNT bundle in the range of 1400 to 1750 cm^{-1} under 532 nm CW laser irradiation. Figure 1 (e) shows one of the Raman spectrum of the CNTs bundles. The Raman intensity of *G* peak against θ is indicated in Fig. 1(d). As shown in Fig. 1(d), the Raman intensity of the *G* peak is maximum near 0° and 180°. The intensity of *G* peak is normalized by the Raman intensity of *G* peak of high purity graphene paper to discard the effects of beam splitter and other optical components of the Raman system [53]. The normalized Raman intensity of the *G* peak is fitted by Eq. (1) to find the orientation distribution $g(\alpha)$ of CNTs. The fitted $g(\alpha)$ function is plotted in Fig. 1(f). As shown in this figure, the probability of finding CNTs aligned with the bundle's axial direction reaches the maximum at 0° and 180°. This value is two times higher than the minimum probability, which happens at 90° and 270°. This sine-wave-like alignment distribution shows that although the majority of the nanotubes are aligned along the bundle's axial direction, a significant amount of them are also aligned in other directions.

3. DTR Phenomenon Discovered in TET Characterization

A. Physics of TET characterization

The DTR phenomenon is discovered during the thermal diffusivity (α) measurement of CNT bundles by using the transient electrothermal (TET) technique [Fig. 2(a)]. The TET technique features strong signal level and fast measurement, and can be applied to metallic, semi-conductive and nonconductive materials.[47, 54-57] The measurement accuracy of this technique has been extensively examined by characterizing known materials, including both metallic and dielectric materials with measurement uncertainty better than ±10%.[47, 54-57] In the experiment, the sample is suspended between two gold coated silicon electrodes on a glass wafer and connected by using a small amount of silver paste. Figure 2(b) shows a microscopy image of the suspended CNT bundle sample. The sample is then placed in a vacuum chamber, where the vacuum level is maintained below 0.5 mTorr. Due to the low air pressure in the chamber, the heat convection by air can be neglected.

Figure 2(a) shows the schematic of the experimental set-up. During TET measurement, a small step current is fed through the sample by a current source to induce fast joule heating, which leads to a fast temperature rise. The corresponding voltage-time profiles (V-t) are collected by using an oscilloscope. In general, the higher α of the sample, the faster temperature evolution and shorter time to reach the steady state. The transient temperature change can be used to determine α of the to-be-measured sample. During this transient process, the heat transfer in the sample can be treated one-dimensional with sound accuracy. The governing equation is expressed as [54, 58]

$$\frac{1}{\alpha}\frac{\partial\theta(x,t)}{\partial t}=\frac{\partial^2\theta(x,t)}{\partial x^2}+\frac{I^2R}{kLA_c}+\frac{Q_{rad}}{kLA_c}. \tag{1}$$

In this equation, $\theta = T - T_0$ is the temperature rise of the sample (T: temperature, T_0: initial temperature), α is the thermal diffusivity, t is time, L and A_c are the suspended length and the cross-

sectional area of the sample, respectively, I is the current passing through the sample, R the resistance of the sample, and Q_{rad} the heat transfer rate of radiation from the sample surface. By integral of Green's function, the normalized temperature rise for this transient state, which is defined as $T^* = \left[T(t) - T_0\right] / \left[T(t \to \infty) - T_0\right]$, can be derived as:[54]

$$T^* \cong \frac{48}{\pi^4} \sum_{m=1}^{\infty} \frac{1-(-1)^m}{m^2} \frac{1-\exp[-m^2\pi^2\alpha_m t / L^2]}{m^2}. \tag{2}$$

Note this normalized temperature rise can also be simplified as $T^* = 1 - 0.99e^{-9.911 \times \alpha_m t / L^2}$ [59]. The small current used for the TET measurement (around 50 mA) induces only a small temperature rise, within which the temperature coefficient of resistance can be assumed constant. Thus, T^* can be obtained by the normalized V-t curve. Figure 2(c) shows a typical V-t curve of the CNT bundle sample obtained at 295 K in the first round of cryogenic experiment, where the signal can be divided into two parts: the transient state and the steady state. This is a normal TET signal for materials with negative temperature coefficient of resistance. Upon the step current heating, the V-t curve presents a fast decreasing behavior due to the joule heating. Then the temperature reaches a steady state, resulting from the energy balance of joule heating, heat conduction and thermal radiation. The normal V-t curve can be very well fitted by using the least square fitting (LSF) method based on Eq. (2) [54] as shown in Fig. 2(c). The trial α value which gives the best fit of the experiment data is taken as the sample's α.

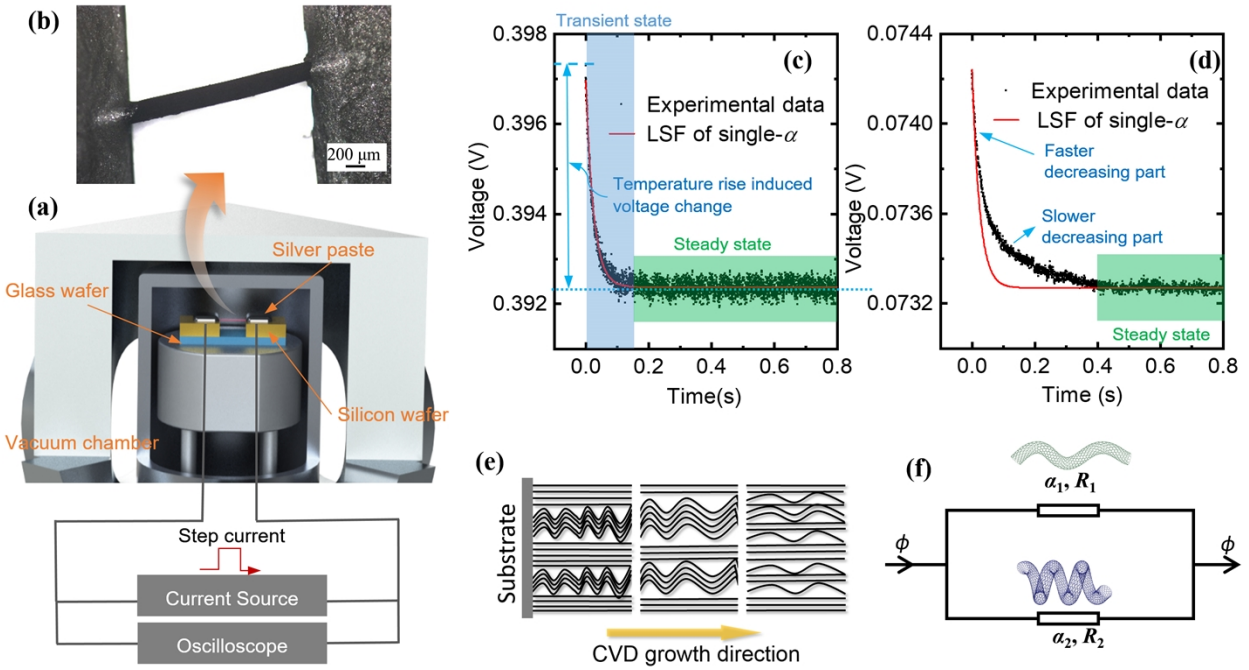

Figure 2. (a) Schematic of the experimental set-up of TET characterization. (b) The suspended CNT bundle sample under optical microscope. (c) A typical *V*-*t* curve from the TET measurement of the sample at 295 K in the first round of cryogenic experiment. It can be fitted by LSF based on the single-α model in Eq. (2) with sound accuracy. (d) One of the *V*-*t* curve where the DTR phenomenon emerges. It cannot be fitted by LSF based on the single-α model in Eq. (2) for the entire curve. (e) A schematic of the macroscopic CNT morphologies where some of the initially straight CNTs develop coiled morphologies due to the competing factors of collective growth and spatial constraints.[16] (f) A schematic showing the parallel heat transfer model in the VACNTs arrays.

B. Discovery of DTR phenomenon and temperature's effect

The DTR phenomenon is first discovered during the cryogenic TET characterization and it only emerges at certain temperatures. To study the thermal properties of CNT bundles at cryogenic temperatures, the sample is put on a cold head in a vacuum chamber (Janis, closed cycle

refrigerator system) where the temperature is controlled to vary from 295 K to 10 K. The TET characterization is conducted every 5-30 K. As temperature goes down to 35 K, we observe a DTR phenomenon. Figure 2(d) shows one of the DTR signals. It can be seen that the *V- t* curve shows a fast decreasing pattern just like that in Fig. 2(c) at the beginning. However, there is an extra slower-decreasing part emerging after the fast-decreasing part. As shown in the figure, this abnormal DTR *V- t* curves cannot be fitted by the LSF based on the model described by Eq. (2), which indicates that the heat transfer process in these situations are more complex than the model presented in Eq. (1) and (2). As will be discussed later, these abnormal processes have nothing to do with electrical inductance or capacitance effect as their magnitude is proportional to the joule heating power, not the electrical current level.

As illustrated in the structure characterization section, two distinctly different CNT morphologies developed in the CNTs arrays. One morphology is relatively straight tubes, while the other is coiled tubes. Figure 2(e) shows a schematic of the root growth mechanism illustrating that some of the initially straight CNTs develop into coiled morphologies in latter stages of growth during CVD process. Based on the structure characteristics and the observed TET signals, we speculate that the observed DTR phenomenon is resulted from two parallel routes of heat conduction in the CNT bundles where the straight and coiled CNTs constitute two parallel heat transport paths for phonons. As illustrated in Fig. 2(f), when heat is conducted from the middle point of the sample to the end, two parallel heat paths are available. α_1 and α_2 correspond to the thermal diffusivity of the straight tubes and the coiled tubes, respectively. R_1 and R_2 are the corresponding electrical resistance of the two strutures, respectively. Below we show how to use this two-pace parallel heat conduction model to fit the experimental data.

In our first round cryogenic experiment, it is discovered that the DTR phenomenon starts to emerge when the temperature is reduced to a certain level. To illustrate this, the normalized temperature rise profiles obtained by the normalized voltage curve as $T^* = \left[V(t) - V_0\right] / \left[V(t \to \infty) - V_0\right]$ at selected temperatures are presented in Fig. 3(a) with offset for comparison. The T^*-t profiles present a normal single-stage temperature increasing pattern at the temperature range of 295 K to 55 K. When the temperature is lowered down to 35 K, they begin to show a DTR pattern: a fast-increasing stage and a slow-increasing stage. The slow-increasing pattern continues to develop in TET when the temperature is further lowered down to 10 K. This DTR pattern cannot be fitted using the TET model as presented in Eq. (2). Instead, a dual-α physical model can be used to fit the DTR data:[59]

$$T^* = Ae^{-9.911 \times \alpha_1 t / L^2} + Be^{-9.911 \times \alpha_2 t / L^2} + C \,. \tag{3}$$

In this model, α_1 and α_2 are two different thermal diffusivities corresponding to two simultaneous heat conduction in CNT bundles. The dual-α model assumes two simultaneous thermal transport processes in CNT bundles and considers them independent of each other. As shown in Fig. 3(a), the model fits the DTR T^*-t curves with excellent accuracy.

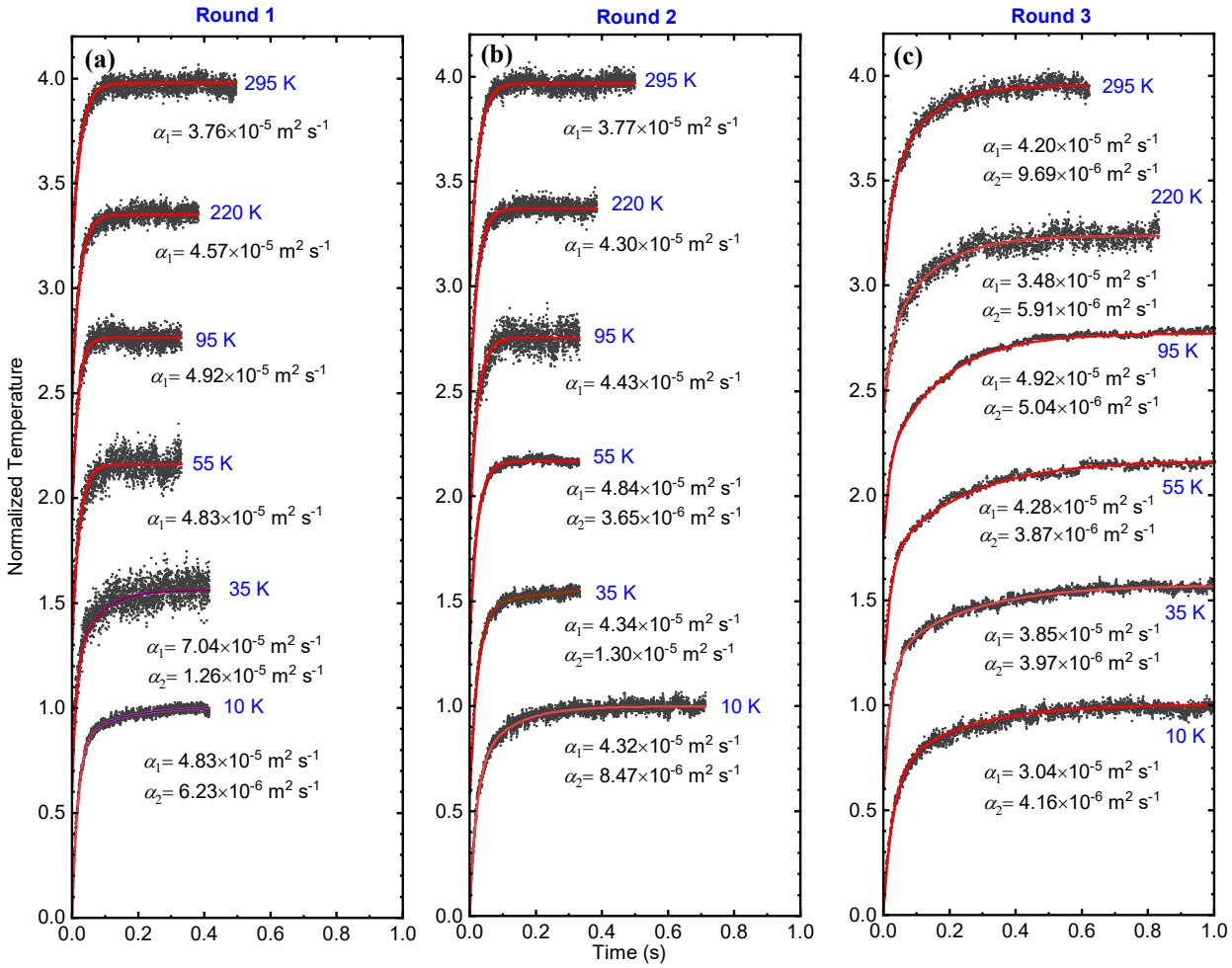

Figure 3. The normalized temperature rise against time curve with offset during TET characterization for the first round (a), the second round (b), and the third round (c) of cryogenic experiment.

To study if the DTR phenomenon induced by low temperature is reversible or not, the same sample is measured for three rounds. In each round of the cryogenic experiment, the temperature of the cold head is lowered down from 295 K to 10 K and then slowly returned to 295 K. The normalized T^*-t data for the second and third round at selected temperatures are shown in Fig. 3(b) and (c), respectively. It is found that the temperature of DTR emergence is different for the three rounds. For the first round, the DTR phenomenon emerges at 35 K. For the second round, the DTR phenomenon starts at 55 K and exists at lower temperatures. For the third round, the DTR phenomenon is observed in the whole temperature range of 295 K to 10 K. The physics for the development of the parallel heat transport path under low temperatures will be investigated in the following sections.

4. DTR Heat Conduction by Structure Separation

A. Dual-mode thermal diffusivity and structure separation

As shown in Fig. 3, the dual-α model fits the V-t curves for the DTR phenomenon in the three round of cryogenic experiment excellently. From this parallel dual-α heat conduction model, two different thermal diffusivity values are determined and denoted correspondingly in Fig. 3. The higher thermal diffusivity is denoted as α_1, and the lower one is denoted as α_2. The α_1 and α_2 results are summarized in Fig. 4(a). For the first round, α_2 first emerges at 35 K; while for the second round, α_2 appears at 55 K and continues to exist when the temperature is reduced to 10 K. For the third round, α_1 and α_2 are both observed in the whole temperature range of 295 K to 10 K. At 295 K, α_1 (3.72- 4.19×10^{-5} m^2 s^{-1}) is 3-4 times higher than that of α_2 (9.91×10^{-6} m^2 s^{-1}). This indicates that for the observed two thermal transport processes illustrated in Fig. 2(f), one transfers heat much faster than the other one.

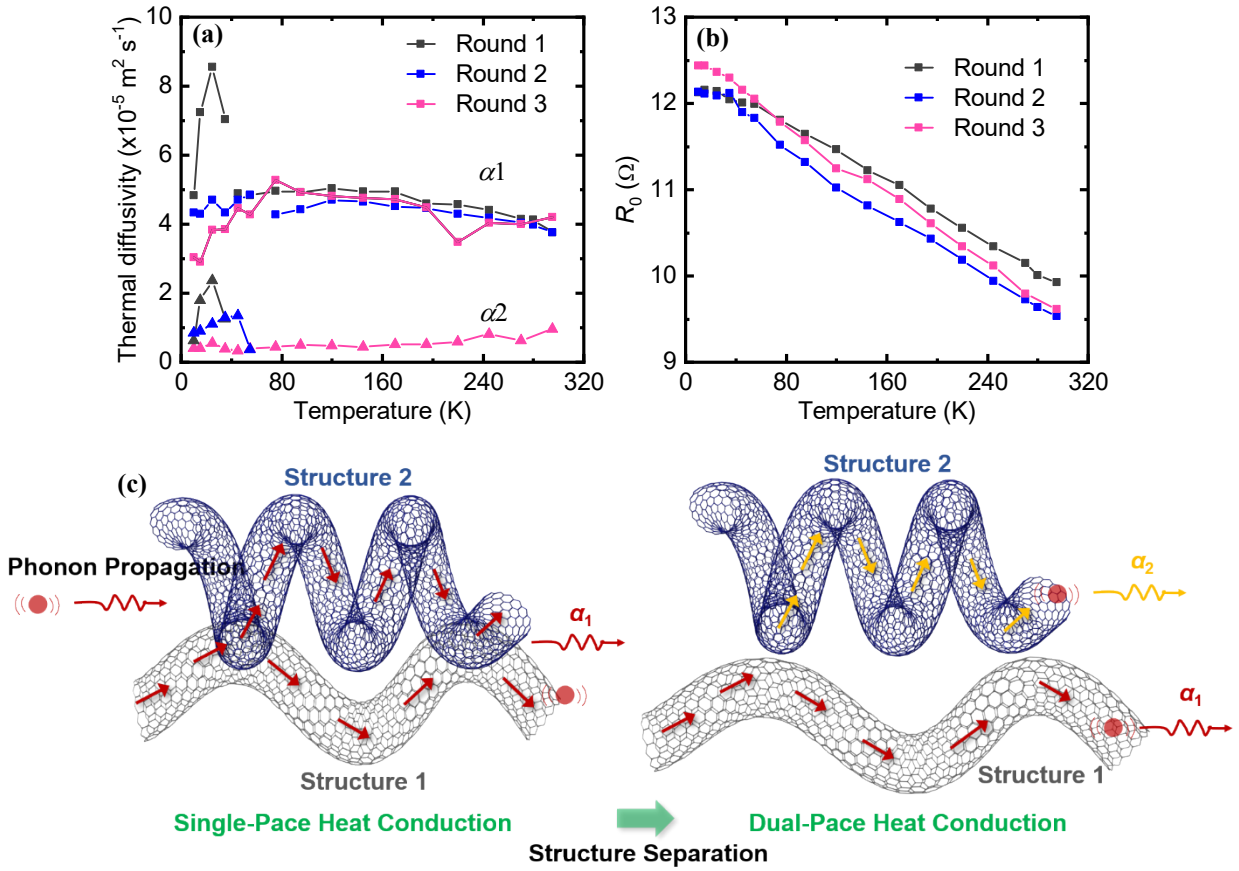

Figure 4 (a) The measured thermal diffusivity. (b) The electrical resistance of the CNTs bundles. (c) The schematic showing the structure separation process of the two CNTs of different morphologies as temperature goes down.

For the one-dimensional heat transfer model expressed in Eq. (2), if an effective sample length (L_e) instead of the real heat conduction length (L_r) is used in data fitting, the determined effective α is proportional to L_e^2/L_r^2. The coil-shaped CNTs have a much longer real heat transfer path than the straight CNTs. Therefore, if we evaluate the heat transfer at the sample length scale (effective length), the effective α of straight CNTs will be much higher than that of coiled CNTs. After evaluating several heat transfer pathes under SEM, the average ratios of the actual heat transfer route of the coiled CNTs over the axial-direction distance in the sample is estimated to be 1.24.

Taking the radial symmetry property of the coiled CNTs into consideration, since $\sqrt{L_x^2+L_y^2}=1.24$, the 3D ratio of the curvatural length of the coilded CNTs over the straight line length can be determined as $\sqrt{L_x^2+L_y^2+L_z^2}=1.52$. Thus, the relationship between the effective thermal diffusivity of the straight CNTs and the coiled CNTs can be calculated as $\alpha_1=1.52^2\times\alpha_2$=$2.31\alpha_2$. In addition, the faster growth speed and higher density of catalyst particles bring in higher density of defects and/or impurities in the coiled CNTs inevitably, which could also contribute to a lower intrinsic α of coiled CNTs. This will make the estimated α_1/α_2 ratio even higher than 2.31, closer to the ratio of 3~4 observed in experiments.

As temperature goes down, α_1 shows a slowly increasing pattern from 3.72- 4.19×10^{-5} m^2 s^{-1} to 2.94- 8.55×10^{-5} m^2 s^{-1}, while α_2 slowly decreases from 9.91×10^{-6} m^2 s^{-1} to about 3.70×10^{-6} m^2 s^{-1}. For an individual CNT, α should increase with the decreased temperature according to the thermal reffusivity theory.[45, 46] Phonons are the main heat carriers in CNT-based materials. During phonon propagation, phonons encounter scattering from not only other phonons (Umklapp scattering), but also structural defects. To participate in the Umklapp process, the energy of phonons needs to be in the order of $k_B\theta/2$, in which k_B is Boltzmann constant, and θ is the Debye temperature.[60] At high temperatures where most phonons are excited, the Umklapp scattering dominates the phonon scattering process. As temperature goes down, the lattice elastic vibration weakens and phonon population decreases. The Umklapp scattering intensity is reduced correspondently, which results in the increased thermal diffusivity.[44-46] While α_1 shows a slowly increasing pattern which agrees well with that of the thermal reffusivity theory, α_2 slowly decreases as temperature goes down from room temperature (RT) to 10 K. This completely

reversed trend of α_2 $-T$ indicates a dominating effect of phonon scattering at interfaces among neighboring CNTs[61]. The CNT-CNT contact in α_2 is worsened greatly by the reduced temperature, which even offsets the significantly increasing intrinsic α pattern with the reduced temperature. Thus, the α–T curve demonstrates that the dominating mechanism for α_1-T variation is the Umklapp scattering, while for α_2 is the interfaces phonon scattering.

Figure 4(b) shows the measured electrical resistance of the sample for the three rounds of experiments. The R_0-T curves for the three rounds of experiments present a very similar linearly increasing pattern as temperature goes down. However, the increasing rate dR/dT becomes a little higher from the first round to the third round of cryogenic experiment. A linear fitting can be used to fit the R_0-T curves for the three rounds of experiments. The fitting result is R_0= 12.35-0.0081T for the first round, R_0= 12.28-0.0096T for the second round, and R_0=12.58-0.010T for the third round of experiment. The slope of the R_0-T curves (dR_0/dT) increases as the cryogenic experiment cycles increase, which indicates R_0 becomes more sensitive to temperature change as the cryogenic experiment cycles increase. Also these R-T relations show that there is no abrupt dR/dT change when T changes. This helps exclude any dR/dT factors in the observed DTR phenomenon.

We speculate that there is a nano-scale structure separation between the relatively straight CNTs and the coiled CNTs in the CNT arrays as temperature goes down, which is responsible for the DTR phenomenon. As shown in Fig. 4(c), the two CNTs of coiled and relatively straight morphology are in good contact by Van der Waals (vdW) force at RT before the cryogenic experiment. As temperature goes down, the negative thermal expansion coefficient of CNTs results in the thermal expansion in the length direction. Due to the coiled morphology, the

expansion of the coiled CNTs is expected to be much smaller than that of the straight ones in the axial direction. Thus, as the thermal strain is built up by the decreased temperature, a thermal expansion mismatch occurs between the two different CNTs, leading to a structure separation at low temperatures (35 K for the first round of cryogenic experiment). For the first round of cryogenic experiment, the structure separation is found to be reversible as temperature is increased up. This is why the *V-t* curves of the second round of experiment are consistent with that of the first round in the temperature range of 295 K to 75 K. However, the DTR phenomenon begins to appear at 55 K in the second round of cryogenic experiment. This indicates the structure separation becomes easier after the first round of cryogenic experiment. In the third round of cryogenic experiment, the DTR phenomena are observed for the whole temperature range from 295 K to 10 K. This illustrates that the structure separation becomes irreversible after the second round of cryogenic experiment. Such structure separation could also happen among CNTs in contact in the axial direction, leading to reduction of the overall thermal conductivity [confirmed in Fig. 5(c)]. However, the structure separation leaves very little effect on the electrical resistance, probably due to the electron tunneling effect at the CNT-CNT contact points.

B. Reduced CNT-CNT contact

To confirm the collected *V-t* signals of DTR in TET characterization are from the joule heating effect, we study the ΔV-I^3 curves at 10 K as an example. For one-dimensional heat transfer along the CNT bundle, the temperature rise in steady state can be derived as $\Delta T = I^2RL/12kA_c$, where I^2R is the joule heating power induced by the step current at steady state, L the suspended length of the sample, and A_c the sample's cross-sectional area.[61-63] It can be seen clearly from this equation that the temperature rise of the sample induced by the joule heating effect is proportional

to the supplied current as: $\Delta T \propto I^2$. In a small temperature range, the change of electrical resistance ΔR can be considered proportional to ΔT. Therefore, if the voltage change in the TET signals is induced by the small joule heating effect, the resulting voltage change [$\Delta V = V(t \to \infty) - V_0$] should be linearly related to I^3 as $\Delta V \propto I^3$. As shown in Fig. 5(a), the absolute value of ΔV at 10 K in the third round of experiment shows a good linear relationship with I^3, which clearly confirms the joule heating effect. Furthermore, for the dual-α physics model in Eq. (3), the coefficient A and B are proportional to the voltage change induced by the two different thermal diffusivities α_1 and α_2 respectively. The corresponding absolute values of A and B resulted from the four different step currents are also presented in Fig. 5(a). It can be seen clearly that both $|A|$ and $|B|$ also show a good linear relationship with I^3. These results firmly demonstrate that the observed DTR signals in the TET experiment are resulted from joule heating.

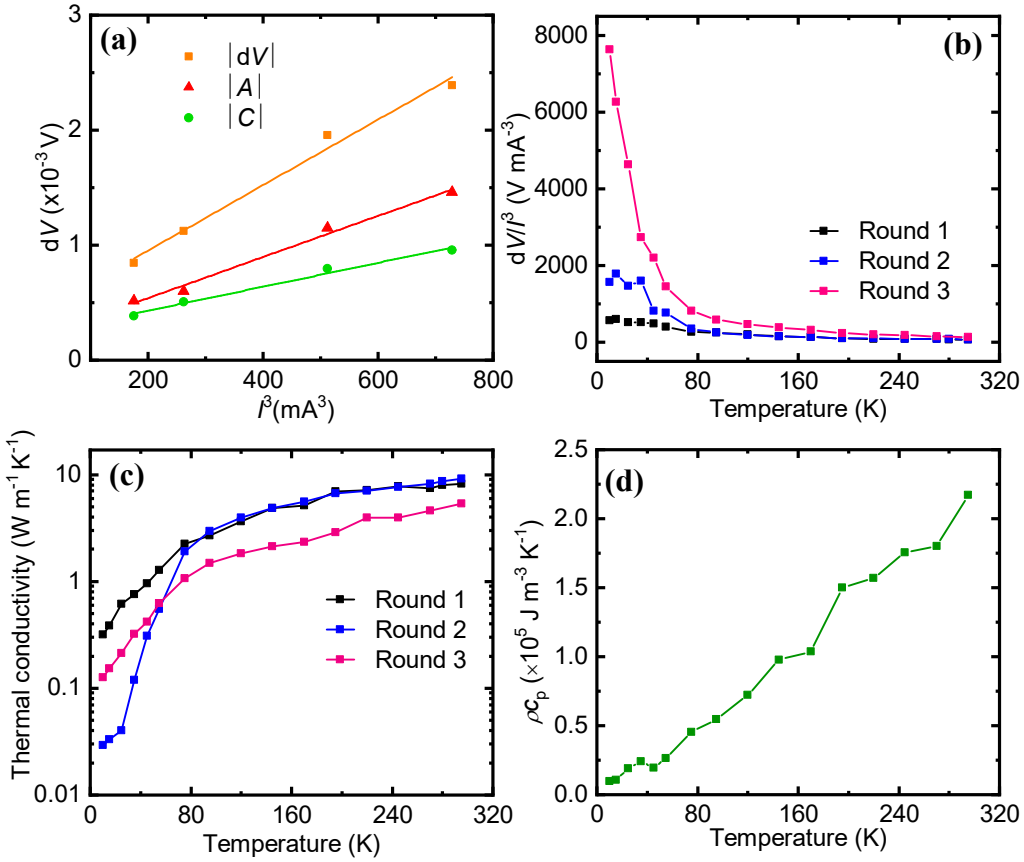

Figure 5 (a) ΔV, $|A|$, and $|B|$ against I^3 at 10 K in the third round of experiment. (b) dV/I^3 against temperature illustrating the reduced CNT-CNT contact. (c) The measured apparent thermal conductivity. (d) The volumetric specific heat of the CNTs bundles from the first round of experiment.

To understand the corresponding micro-structure evolution governing this DTR process, the dV/I^3 against temperature curves are calculated. As presented in Fig. 5(b), dV/I^3 increases as temperature goes down. For the first round of cryogenic experiment, dV/I^3 slowly increases from 70.36 V mA^{-3} at 295 K to 569.51 V mA^{-3} at 10 K, which is 8-fold increase. For the second round of cryogenic experiment, dV/I^3 shows a faster increase from 70.36 V mA^{-3} at 295 K to 1572.19 V mA^{-3} at 10 K, which is 22-fold increase. For the third round of experiment, dV/I^3 increases sharply from 116.67

V mA^{-3} at 295 K to 7630.54 V mA^{-3} at 10 K, which is 65-fold increase. The overall voltage change is $dV = I \cdot \Delta R = I \cdot \Delta T \cdot dR/dT$. At steady state, we have $\Delta T = I^2 RL/(12A_c \cdot k)$. Therefore, $dV/I^3 = RL\,dR/dT/(12A_c \cdot k)$, where A_c is the cross-sectional area of the sample. As shown in Fig. 4(b), R and dR/dT change little from round 1 to round 3. Therefore the changes of dV/I^3 from round 1 to round 3 mostly are induced by the change of thermal conductivity k. The joule heating during TET characterization can reverse some of the structure separation while the number of contacts that can be recovered is limited. This explains the significantly increased dV/I^3 uncovered in the experiments.

The apparent thermal conductivity (k_m) is characterized by using the steady-state electro-thermal (SET) technique.[61-63] The experimental set-up is same as that of the TET technique. In this method, k at each temperature is obtained by: $k_m = I^2 RL(dR/dT)/12A_c \Delta R$. In the equation, k_m is the apparent thermal conductivity, I the DC current flowing through the sample, R the resistance of the sample at steady state, dR/dT is obtained by differentiating the R_0-T curve, and ΔR the resistance change induced by the joule heating. The resulting thermal radiation effect is calculated and found to take less than 2% of k_m. Therefore, the error from the thermal radiation effect is insignificant on the final result. The measurement uncertainty of SET is estimated to be about ±10%. For clarity of comparison, the error bars are omitted in the figure.

Figure 5(c) shows the result of k_m for the three rounds of cryogenic experiments. In the first round, k_m undergoes a decreasing pattern from 9.14 W m^{-1} K^{-1} to 0.32 W m^{-1} K^{-1} as temperature goes down from 295 K to 10 K, which shows a quartic relation with temperature. In the second round of cryogenic experiment, the measured k_m presents a good consistency with that of the first round

in the temperature range of 295 K to 75 K. However, as temperature is further lowered down to 55 K, k begins to drop fast and significantly deviates from k_m of the first round, which decreases from 1.90 W m^{-1} K^{-1} at 75 K to 0.03 W m^{-1} K^{-1} at 10 K. For the third round of experiment, k decreases from 5.32 W m^{-1} K^{-1} to 0.13 W m^{-1} K^{-1}, following a quartic relation with temperature, which is a very similar decreasing pattern as that of the first round. Nevertheless, the value of k_m is 1.72-2.55 times lower than that of the first round in the whole temperature range of 295 K to 10 K. This indicates the micro-structure of the CNT array undergoes an irreversible change after the second round of cryogenic experiment. The volumetric specific heat (ρc_p) against temperature profile is obtained using the measured thermal diffusivity α_1 and measured thermal conductivity k_m in the first round of experiment as $\rho c_p = k_m/\alpha_m$. Figure 5(d) shows the resulting volumetric specific heat. ρc_p decreases linearly with the trend similar to that of graphite. As temperature goes to zero, the specific heat goes to zero. Since α_1 is dominated by the intrinsic thermal properties of the CNTs as illustrated in the thermal diffusivity discussion above, this result demonstrates the good accuracy of the k_m and α_m result.

C. The parallel heat transfer model

In this section, the proportion of the straight CNTs and coiled CNTs under different temperatures will be investigated to have a closer look at the structure evolution. For the two parallel resistances R_1 and R_2 as shown in Fig. 2(f), we have:

$$\Delta R = \frac{\Delta R_1 R_2^2}{(R_1 + R_2)^2} + \frac{\Delta R_2 R_1^2}{(R_1 + R_2)^2}. \tag{4}$$

If the temperature coefficient of resistance for the two parallel resistances is assume to be β_1 and β_2, respectively, the overall temperature coefficient of resistance (dR/dT) can be derived as:

$$\frac{dR}{dT} = \frac{\beta_1 R_2^2}{(R_1 + R_2)^2} + \frac{\beta_2 R_1^2}{(R_1 + R_2)^2}. \tag{5}$$

Thus, the overall temperature change (ΔT) due to joule heating, which is obtained as ΔT=ΔR/(dR/dT), can be derived by combining Eq. (4) and (5) as:

$$\Delta T = \frac{\Delta R_1 R_2^2 + \Delta R_2 R_1^2}{\beta_1 R_2^2 + \beta_2 R_1^2}. \tag{6}$$

Since for the two resistance, ΔR_1= $\Delta T_1 \cdot \beta_1$ and ΔR_2= $\Delta T_2 \cdot \beta_2$, we have:

$$\Delta T = \frac{\beta_1 R_2^2 \Delta T_1 + \beta_2 R_1^2 \Delta T_2}{\beta_1 R_2^2 + \beta_2 R_1^2}. \tag{7}$$

For each heat transfer path, its temperature rise is $\Delta T = V^2 L / (12 R A_c k)$. Here L and A_c are the real heat transfer length and cross-sectional area, respectively. If we assume the two structures have the same intrinsic thermal conductivity and electrical resistivity, and their only difference is the morphology, then we have $\Delta T_1 = \Delta T_2$. Such assumption is physically reasonable since the two structures follow the same growth mechanisms. This conclusion also tells that during the dual-path heat conduction, there is no heat exchange between the two structures. Then it can be seen clearly that the overall temperature rise is equal to that of the two parallel resistances, ΔT= ΔT_1 =ΔT_2.

During the TET characterization, dV is related to I as $dV = I \cdot \Delta R$. Combined with Eq. (4), we have:

$$\Delta V = \frac{I_0 \Delta R_1 R_2^2}{(R_1 + R_2)^2} + \frac{I_0 \Delta R_2 R_1^2}{(R_1 + R_2)^2}. \tag{8}$$

Since ΔR_1 =$\Delta T \cdot \beta_1$ and ΔR_2 =$\Delta T \cdot \beta_2$, and it has been demonstrated above that the overall temperature rise is equal to that of the two parallel resistances, ΔT= ΔT_1 =ΔT_2, the voltage change can be derived as:

$$\Delta V = I_0 \Delta T \frac{\beta_1 R_2^2}{(R_1 + R_2)^2} + I_0 \Delta T \frac{\beta_2 R_1^2}{(R_1 + R_2)^2}. \quad (9)$$

Combining the dual-α thermal transport model in Eq. (3), for the two different morphologies of CNTs, we have $A \propto I_0 \Delta T \beta_1 R_2^2 / (R_1 + R_2)^2$ and $B \propto I_0 \Delta T \beta_2 R_1^2 / (R_1 + R_2)^2$. Therefore, the ratio A/C can be expressed as $A/C = (\beta_1/\beta_2) \cdot (R_2^2/R_1^2)$. As shown in Fig. 6(a), A/C is less than 1 in the temperature range of 55 K to 295 K, while it increases to more than 2 at temperatures below 15 K. This result indicates that although R_2 is larger than R_1, the increasing rate of R_2 is faster than that of R_1, which makes β_2 much higher than β_1 at relatively high temperatures. This is because structure 2 has fewer CNT-CNT contacts than structure 1. The much higher β_2 results in the ratio of A/C less than 1. While at very low temperatures (below 55 K), since the value of R_2 increases to very high value, the term (R_2^2/R_1^2) becomes dominating in A/C, which makes A/C increases to a value higher than 2.

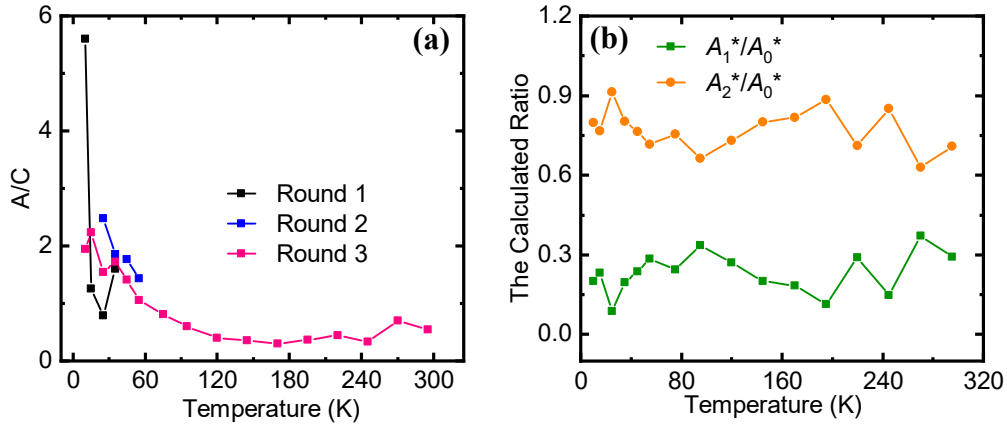

Figure 6 (a) The ratio of A/C and (b) the ratio of the calculated normalized area of the two different CNTs for the further analysis of the nano-scale structure separation.

If we assume that that the total cross-sectional area of the CNTs bundle is A, the proportion that structure 1 (relatively straight CNTs) takes is A_1^*, and the proportion that structure 2 (coiled CNTs) takes is A_2^*, then the real cross-sectional area of structure 1 and structure 2 is $A_1 = A \cdot A_1^*$ and $A_2 = A \cdot A_2^*$, respectively. Note A for the total CNT bundle includes the effect of open space among CNTs. A_1 and A_2 for the relatively stright and coiled CNTs are only for the area of the solid part. Also we assume the real heat transfer path of structure 1 and structure 2 is L_1 and L_2, respectively. For the one-dimensional heat transfer model in steady state, the apparent thermal conductivity can be derived as $k_{\text{eff}} = (V^2/R) \cdot L/(12\Delta TA)$, where V^2/R is the joule heating power induced by the step current, L is the suspended length of the sample.[61, 62] Combined with the parallel resistance model, by simple mathematical derivation, k_{eff} can be expressed as:

$$k_{eff} = \frac{V^2 L_1}{12 A_1 \Delta T \cdot R_1} \cdot \frac{A_1}{A} \cdot \frac{L}{L_1} + \frac{V^2 L_2}{12 A_2 \Delta T R_2} \cdot \frac{A_2}{A} \cdot \frac{L}{L_2}. \tag{10}$$

In addition, from Eq. (2), it can be seen clearly that the effective thermal diffusivity is reversely proportional to the square of real heat transfer length, which leads to $\sqrt{\alpha_1} \propto L / L_1$ and $L / L_2 \propto \sqrt{\alpha_2}$. For the one-dimensional heat transfer model in steady state, the intrinsic thermal conductivity of structure 1 and structure 2 can also be expressed as $k_1 = (V^2/R_1)L_1/(12A_1\Delta T)$ and $k_2 = (V^2/R_2)L_2/(12A_2\Delta T)$. The intrinsic thermal conductivity k_1 and k_2 can be regarded as equal to a constant k. Therefore, after the structure separation, k_{eff} can be expressed as

$$k_{eff,2} = CA_1^* \sqrt{\alpha_1} + CA_2^* \sqrt{\alpha_2}, \tag{11}$$

where $C \propto k$ is a constant. While before the structure separation, we have

$$k_{eff,1} = CA_0^* \sqrt{\alpha_1}, \tag{12}$$

where $A_0^* = A_1^* + A_2^*$ is the total cross-sectional area. By combining Eq. (11) and (12), using the experimental data of apparent thermal conductivity from the first round of cryogenic experiment as $k_{\text{eff},1}$ (before structure separation) and that from the third round of cryogenic experiment as $k_{\text{eff},2}$ (after structure separation), the ratio of the normalized cross-sectional area of structure 1 and structure 2 can be calculated. Figure 6(b) presents the results of A_1^*/A_0^* and A_2^*/A_0^*. It can be seen that A_1^*/A_0^* stays almost constant at around 0.2, while A_2^*/A_0^* at around 0.8. This indicates that after the structure separation, the proportion of structure 1 in the cross section is about 20% while that of structure 2 is about 80%. Therefore, the coiled CNTs play a dominating role in the thermal conduction process of the CNTs bundles after the structure separation. As shown in Fig. 4(c), before structure separation (round 1 and round 2), structure 1 (relatively straight CNTs) are in good contact with the coiled ones. This provides some shortcuts of heat conduction in structure 2. Thus, heat does not have to flow over a long distance in the coiled CNTs. Nevertheless, after the structure separation, heat has to flow in the coiled CNTs, making the effective thermal diffusivity and conductivity lower.

5. Conclusion

In this work, an abnormal DTR phenomenon in vertically aligned CNT arrays was discovered under TET characterization. Three rounds of cryogenic experiments were conducted to confirm and investigate the emergence of the DTR phenomenon. As temperature decreased, the DTR phenomenon emerged at a certain temperature and existed over the lower temperatures. Such phenomenon became permanent over all the temperatures of 295 K to 10 K after two rounds of cryogenic experiments. The voltage change in TET signals was found to be linearly related to I^3, confirming the DTR phenomenon was induced by joule heating. The DTR voltage-time profiles

can be fitted using two thermal diffusivities, reflecting a dual-pace transient thermal response. As temperature went down, the larger thermal diffusivity (α_1) showed a slowly increasing pattern from 3.72- 4.19×10^{-5} m^2 s^{-1} to 2.94- 8.55×10^{-5} m^2 s^{-1}, while the smaller thermal diffusivity (α_2) slowly decreased from 9.91×10^{-6} m^2 s^{-1} to about 3.70×10^{-6} m^2 s^{-1}. The unique structure of CNT bundles constitutes parallel heat conduction paths which result in DTR. The nano-scale structure separation induced by the increased thermal strain led to a thermal diffusivity/conductivity separation phenomenon. To understand the corresponding micro-structure evolution governing this DTR process, the dV/I^3 against temperature curves were calculated. The significantly increased dV/I^3 in the experiments uncovered the reduced CNT-CNT contact as temperature went down. The measured thermal conductivity variation against temperature also supported the proposed structure separation model. By further building a new parallel heat transfer model taking both the transient and steady-state electrical and thermal response into consideration, the ratio of the cross-sectional area of the separated two different CNTs was determined. It was found that the coiled CNTs played a dominant role in the thermal conduction process of the CNT bundle after the structure separation. Our findings uncovered that coiled CNTs and nano-structure evolution of CNTs could have significant effect on the thermal and electrical transport of CVD grown CNTs arrays, especially their transient responses. The developed parallel heat transfer model will be of great value in analyzing experimental results and designing CNTs arrays for various applications.

ACKNOWLEDGMENT

Support of this work by National Natural Science Foundation of China (No. 51906161), Natural Science Foundation of Guangdong Province (No. 2020A1515011186), the Start-up Fund of Shenzhen University and Scientific Research Foundation for Talented Scholars in Shenzhen is gratefully acknowledged. X.W is grateful for the support by US National Science Foundation (CBET1930866 and CMMI2032464). The work by G.E. was supported by the U.S. Department of Energy (DOE), Office of Science, Basic Energy Sciences (BES), Materials Sciences and Engineering Division.

References

[1] E. Pop, D. Mann, Q. Wang, K.E. Goodson, H.J. Dai, Thermal Conductance of an Individual Single-Wall Carbon Nanotube above Room Temperature, Nano Letters 6(1) (2006) 96-100.
[2] C. Silvestri, M. Riccio, R.H. Poelma, A. Jovic, B. Morana, S. Vollebregt, A. Irace, G.Q. Zhang, P.M. Sarro, Effects of Conformal Nanoscale Coatings on Thermal Performance of Vertically Aligned Carbon Nanotubes, Small 14(20) (2018) e1800614.
[3] Y. Cohen, S.K. Reddy, Y. Ben-Shimon, A. Ya'akobovitz, Height and Morphology Dependent Heat Dissipation of Vertically Aligned Carbon Nanotubes, Nanotechnology 30(50) (2019) 505705.
[4] B.R. Lettiere, C.A.C. Chazot, K.H. Cui, A.J. Hart, High-Density Carbon Nanotube Forest Growth on Copper Foil for Enhanced Thermal and Electrochemical Interfaces, ACS Applied Nano Materials 3(1) (2020) 77-83.
[5] Y. Yang, L. Liu, Y. Wei, P. Liu, K. Jiang, Q. Li, S. Fan, In Situ Fabrication of HFC-Decorated Carbon Nanotube Yarns and Their Field-Emission Properties, Carbon 48(2) (2010) 531-537.
[6] W. Li, J. Yuan, A. Dichiara, Y. Lin, J. Bai, The Use of Vertically Aligned Carbon Nanotubes Grown on SiC for in Situ Sensing of Elastic and Plastic Deformation in Electrically Percolative Epoxy Composites, Carbon 50(11) (2012) 4298-4301.
[7] P. La Torraca, M. Bobinger, M. Servadio, P. Pavan, M. Becherer, P. Lugli, L. Larcher, On the Frequency Response of Nanostructured Thermoacoustic Loudspeakers, Nanomaterials 8(10) (2018) 833.
[8] L. Xiao, Z. Chen, C. Feng, L. Liu, Z.Q. Bai, Y. Wang, L. Qian, Y.Y. Zhang, Q.Q. Li, K.L. Jiang, S.S. Fan, Flexible, Stretchable, Transparent Carbon Nanotube Thin Film Loudspeakers, Nano Letters 8(12) (2008) 4539-4545.
[9] P. Liu, L. Liu, Y. Wei, K. Liu, Z. Chen, K.L. Jiang, Q.Q. Li, S.S. Fan, Fast High-Temperature Response of Carbon Nanotube Film and Its Application as An Incandescent Display, Adv Mater 21(35) (2009) 3563-3566.
[10] Z. Yin, H. Wang, M. Jian, Y. Li, K. Xia, M. Zhang, C. Wang, Q. Wang, M. Ma, Q. Zheng, Y. Zhang, Extremely Black Vertically Aligned Carbon Nanotube Arrays for Solar Steam Generation, ACS Applied Materials & Interfaces 9(34) (2017) 28596-28603.
[11] S. Murata, M. Imanishi, S. Hasegawa, R. Namba, Vertically Aligned Carbon Nanotube Electrodes for High Current Density Operating Proton Exchange Membrane Fuel Cells, Journal of Power Sources 253 (2014) 104-113.
[12] K. Jiang, Q. Li, S. Fan, Nanotechnology: Spinning Continuous Carbon Nanotube Yarns - Carbon Nanotubes Weave Their Way into A Range of Imaginative Macroscopic Applications, Nature 419(6909) (2002) 801-801.
[13] M. Zhang, K.R. Atkinson, R.H. Baughman, Multifunctional Carbon Nanotube Yarns by Downsizing An Ancient Technology, Science 306(5700) (2004) 1358-1361.
[14] C.J. Lee, K.H. Son, J. Park, J.E. Yoo, Y. Huh, J.Y. Lee, Low Temperature Growth of Vertically Aligned Carbon Nanotubes by Thermal Chemical Vapor Deposition, Chemical Physics Letters 338(2-3) (2001) 113-117.
[15] K. Jiang, J. Wang, Q. Li, L. Liu, C. Liu, S. Fan, Superaligned Carbon Nanotube Arrays, Films, and Yarns: A Road to Applications, Adv Mater 23(9) (2011) 1154-1161.
[16] H. Wang, Z. Xu, G. Eres, Order in Vertically Aligned Carbon Nanotube Arrays, Applied Physics Letters 88(21) (2006) 213111.
[17] D. Wang, Y. Lei, W. Jiao, Y. Liu, C. Mu, X. Jian, A Review of Helical Carbon Materials Structure, Synthesis and Applications, Rare Metals 40(1) (2020) 3-19.

[18] C.J. Lee, J. Park, S. Han, J. Ihm, Growth and Field Emission of Carbon Nanotubes on Sodalime Glass at 550 Degrees C using Thermal Chemical Vapor Deposition, Chemical Physics Letters 337(4-6) (2001) 398-402.
[19] L. Li, L. Lu, S. Qi, Preparation, Characterization and Microwave Absorption Properties of Porous Nickel Ferrite Hollow Nanospheres/Helical Carbon Nanotubes/Polypyrrole Nanowires Composites, Journal of Materials Science-Materials in Electronics 29(10) (2018) 8513-8522.
[20] Y. Gao, F. Guo, P. Cao, J. Liu, D. Li, J. Wu, N. Wang, Y. Su, Y. Zhao, Winding-Locked Carbon Nanotubes/Polymer Nanofibers Helical Yarn for Ultrastretchable Conductor and Strain Sensor, ACS Nano 14(3) (2020) 3442-3450.
[21] W. Chen, J. Zhang, Y. Yue, Molecular Dynamics Study on Thermal Transport at Carbon Nanotube Interface Junctions: Effects of Mechanical Force and Chemical Functionalization, International Journal of Heat and Mass Transfer 103 (2016) 1058-1064.
[22] K. Bui, B.P. Grady, D.V. Papavassiliou, Heat Transfer in High Volume Fraction CNT Nanocomposites: Effects of Inter-Nanotube Thermal Resistance, Chemical Physics Letters 508(4-6) (2011) 248-251.
[23] C. Nan, G. Liu, Y. Lin, M. Li, Interface Effect on Thermal Conductivity of Carbon Nanotube Composites, Applied Physics Letters 85(16) (2004) 3549-3551.
[24] A.K. Vallabhaneni, B. Qiu, J.N. Hu, Y.P. Chen, A.K. Roy, X.L. Ruan, Interfacial Thermal Conductance Limit and Thermal Rectification across Vertical Carbon Nanotube/Graphene Nanoribbon-Silicon Interfaces, J Appl Phys 113(6) (2013) 064311.
[25] C. Deng, C. Li, P. Wang, X. Wang, L. Pan, Revealing the Linear Relationship Between Electrical, Thermal, Mechanical and Structural Properties of Carbon Nanocoils, Phys Chem Chem Phys 20(19) (2018) 13316-13321.
[26] Y. Xie, T. Wang, B. Zhu, C. Yan, P. Zhang, X. Wang, G. Eres, 19-Fold Thermal Conductivity Increase of Carbon Nanotube Bundles toward High-End Thermal Design Applications, Carbon 139 (2018) 445-458.
[27] C. Yu, G. Zhang, The Underestimated Thermal Conductivity of Graphene in Thermal-Bridge Measurement: A Computational Study, J Appl Phys 113(21) (2013) 214304.
[28] T. Borca-Tasciuc, A.R. Kumar, G. Chen, Data Reduction in 3ω Method for Thin-Film Thermal Conductivity Determination, Review of Scientific Instruments 72(4) (2001) 2139-2147.
[29] M. Sheindlin, D. Halton, M. Musella, C. Ronchi, Advances in the Use of Laser-Flash Techniques for Thermal Diffusivity Measurement, Review of Scientific Instruments 69(3) (1998) 1426-1436.
[30] Y. Yue, X. Huang, X. Wang, Thermal Transport in Multiwall Carbon Nanotube Buckypapers, Physics Letters A 374(40) (2010) 4144-4151.
[31] Y. Hu, A. Fan, H. Wang, W. Ma, X. Zhang, Dual-Wavelength Flash Raman Mapping Method for Measuring Thermal Diffusivity of the Suspended Nanowire, Science China-Technological Sciences 63(5) (2020) 748-754.
[32] A. Fan, Y. Hu, H. Wang, W. Ma, X. Zhang, Dual-Wavelength Flash Raman Mapping Method for Measuring Thermal Diffusivity of Suspended 2D Nanomaterials, International Journal of Heat and Mass Transfer 143 (2019) 118460.1-118460.9.
[33] R. Wang, S. Xu, Y. Yue, X. Wang, Thermal Behavior of Materials in Laser-Assisted Extreme Manufacturing: Raman-Based Novel Characterization, International Journal of Extreme Manufacturing 2 (2020) 032004.

[34] M. Bauer, Q. Pham, C. Saltonstall, P. Norris, Thermal Conductivity of Vertically Aligned Carbon Nanotube Arrays: Growth Conditions and Tube Inhomogeneity, Applied Physics Letters 105(15) (2014) 2608-1243.
[35] X. Huang, J. Wang, G. Eres, X. Wang, Thermophysical Properties of Multi-Wall Carbon Nanotube Bundles at Elevated Temperatures Up to 830 K, Carbon 49(5) (2011) 1680-1691.
[36] I. Ivanov, A. Puretzky, G. Eres, H. Wang, Z.W. Pan, H.T. Cui, R.Y. Jin, J. Howe, D.B. Geohegan, Fast and Highly Anisotropic Thermal Transport through Vertically Aligned Carbon Nanotube Arrays, Applied Physics Letters 89(22) (2006) 223110.
[37] D. Yang, Q. Zhang, G. Chen, S.F. Yoon, J. Ahn, S. Wang, Q. Zhou, Q. Wang, J. Li, Thermal Conductivity of Multiwalled Carbon Nanotubes, Physical Review B 66(16) (2002) 165440.
[38] J. Hone, M. Whitney, C. Piskoti, A. Zettl, Thermal Conductivity of Single-Walled Carbon Nanotubes, Synthetic Metals 103(4) (1999) 2514-2516.
[39] J. Wang, M. Gu, X. Zhang, G. Wu, Measurements of Thermal Effusivity of A Fine Wire and Contact Resistance of A Junction Using A T Type Probe, Review of Scientific Instruments 80(7) (2009) 076107
[40] J. Yang, S. Waltermire, Y. Chen, A.A. Zinn, T.T. Xu, D. Li, Contact Thermal Resistance between Individual Multiwall Carbon Nanotubes, Applied Physics Letters 96(2) (2010) 023109.1-023109.3.
[41] Q. Li, K. Katakami, T. Ikuta, M. Kohno, X. Zhang, K. Takahashi, Measurement of Thermal Contact Resistance between Individual Carbon Fibers Using A Laser-Flash Raman Mapping Method, Carbon 141 (2019) 92-98.
[42] H. Zhang, J. Li, K. Yao, L. Chen, Spark Plasma Sintering and Thermal Conductivity of Carbon Nanotube Bulk Materials, J Appl Phys 97(11) (2005) 56.
[43] J. Guo, X. Wang, D.B. Geohegan, G. Eres, C.c. Vincent, Development of pulsed laser-assisted thermal relaxation technique for thermal characterization of microscale wires, Journal of Applied Physics 103(11) (2008) 113505.
[44] C. Deng, Y. Sun, L. Pan, T. Wang, Y. Xie, J. Liu, B. Zhu, X. Wang, Thermal Diffusivity of A Single Carbon Nanocoil: Uncovering the Correlation with Temperature and Domain Size, ACS Nano 10(10) (2016) 9710-9719.
[45] Y. Xie, B. Zhu, J. Liu, X.U. Zaoli, X. Wang, Thermal Reffusivity: Uncovering Phonon Behavior, Structural Defects, and Domain Size, Frontiers in energy 12(1) (2018) 143-157.
[46] Y. Xie, Z. Xu, S. Xu, Z. Cheng, N. Hashemi, C. Deng, X. Wang, The Defect Level and Ideal Thermal Conductivity of Graphene Uncovered by Residual Thermal Reffusivity at the 0 K Limit, Nanoscale 7(22) (2015) 10101-10110.
[47] Z. Xu, X. Wang, H. Xie, Promoted Electron Transport and Sustained Phonon Transport by DNA Down to 10 K, Polymer 55(24) (2014) 6373-6380.
[48] Z. Cheng, Z. Xu, S. Xu, X. Wang, Temperature Dependent Behavior of Thermal Conductivity of Sub-5 Nm Ir Film: Defect-Electron Scattering Quantified by Residual Thermal Resistivity, J Appl Phys 117(2) (2015) 024307.
[49] A. Nag, M.E.E. Alahi, S.C. Mukhopadhyay, Z. Liu, Multi-Walled Carbon Nanotubes-Based Sensors for Strain Sensing Applications, Sensors 21(4) (2021) 1261.
[50] D. Zhang, Z. Shao, D. Geng, X. Jiang, Y. Liu, Z. Zhou, S. Li, Feasibility Study of Wave-Motion Milling of Carbon Fiber Reinforced Plastic Holes, International Journal of Extreme Manufacturing 3 (2021) 010401.

[51] G. Eres, A.A. Puretzky, D.B. Geohegan, H. Cui, In Situ Control of the Catalyst Efficiency in Chemical Vapor Deposition of Vertically Aligned Carbon Nanotubes on Predeposited Metal Catalyst Films, Applied Physics Letters 84(10) (2004) 1759-1761.
[52] J.-C. Blancon, M. Paillet, H.N. Tran, X.T. Than, S.A. Guebrou, A. Ayari, A. San Miguel, N.-M. Phan, A.-A. Zahab, J.-L. Sauvajol, Direct Measurement of the Absolute Absorption Spectrum of Individual Semiconducting Single-Wall Carbon Nanotubes, Nature communications 4(1) (2013) 1-8.
[53] H. Zobeiri, R. Wang, C. Deng, Q. Zhang, X. Wang, Polarized Raman of Nanoscale Two-Dimensional Materials: Combined Optical and Structural Effects, The Journal of Physical Chemistry C 123(37) (2019) 23236-23245.
[54] J. Guo, X. Wang, t. Wang, Thermal Characterization of Microscale Conductive and Nonconductive Wires Using Transient Electrothermal Technique, J Appl Phys 101 (2007) 063537
[55] H. Lin, S. Xu, Y. Zhang, X. Wang, Electron Transport and Bulk-like Behavior of Wiedemann-Franz Law for Sub-7 nm-Thin Iridium Films on Silkworm Silk, ACS Applied Materials & Interfaces 6(14) (2014) 11341-11347.
[56] J. Liu, T.Y. Wang, S. Xu, P.Y. Yuan, X. Xu, X.W. Wang, Thermal Conductivity of Giant Mono- to Few-Layered CVD Graphene Supported on An Organic Substrate, Nanoscale 8(19) (2016) 10298-10309.
[57] Z. Cheng, M. Han, P. Yuan, S. Xu, B.A. Cola, X. Wang, Strongly Anisotropic Thermal and Electrical Conductivities of A Self-Assembled Silver Nanowire Network, RSC Advances 6(93) (2016) 90674-90681.
[58] X. Feng, X. Huang, X. Wang, Nonlinear Effects in Transient Electrothermal Characterization of Anatase TiO2 Nanowires, Review of Scientific Instruments 83(4) (2012) 044901.
[59] Y. Xie, P. Yuan, T. Wang, N. Hashemi, X. Wang, Switch on the High Thermal Conductivity of Graphene Paper, Nanoscale 8(40) (2016) 17581-17597.
[60] D.F. Holcomb, Kittel,C - Introduction to Solid State Physics, American Journal of Physics 35(6) (1967) 547-548.
[61] Y. Xie, S. Xu, Z. Xu, H. Wu, C. Deng, X. Wang, Interface-Mediated Extremely Low Thermal Conductivity of Graphene Aerogel, Carbon 98 (2016) 381-390.
[62] Z. Cheng, L. Liu, S. Xu, M. Lu, X. Wang, Temperature Dependence of Electrical and Thermal Conduction in Single Silver Nanowire, Scientific Reports 5 (2015) 10718.
[63] Y. Xie, M. Han, R. Wang, H. Zobeiri, X. Deng, P. Zhang, X. Wang, Graphene Aerogel Based Bolometer for Ultrasensitive Sensing from Ultraviolet to Far-Infrared, ACS Nano 13(5) (2019) 5385-5396.